

Cite this: *J. Mater. Chem.*, 2012, **22**, 17210

www.rsc.org/materials

PAPER

## Zinc stannate nanocubes and nanourchins with high photocatalytic activity for methyl orange and 2,5-DCP degradation†

Zhenfei Tian, Changhao Liang,\* Jun Liu, Hemin Zhang and Lide Zhang

Received 18th April 2012, Accepted 2nd July 2012

DOI: 10.1039/c2jm32406g

Nanomaterials have emerged as remarkable photocatalysts. In this report, multifunctional cube-like  $\text{Zn}_2\text{SnO}_4$  and urchin-like  $\text{ZnSnO}_3$  nanomaterials were successfully synthesized using zinc and tin metals as ablation targets by the combined strategy of laser ablation in liquid and hydrothermal treatment. Addition of ammonia to the hydrothermal reaction can not only tune the phase structure of the final products from cubic spinel-type  $\text{Zn}_2\text{SnO}_4$  to face-centered perovskite  $\text{ZnSnO}_3$  but also control the morphology of  $\text{ZnSnO}_3$  in a concentration-dependent manner. When the ammonia concentration was set to  $3.0 \text{ mol L}^{-1}$ , uniform urchin-like Zn-deficient  $\text{ZnSnO}_3$  with remarkable lattice distortion was obtained. Photocatalytic activity tests using methyl orange (MO) and 2,5-dichlorophenol (2,5-DCP) as probe molecules under ultraviolet light excitation demonstrated that urchin-like  $\text{ZnSnO}_3$  is highly active and effective for the degradation of high concentrations of MO (25 ppm) and 2,5-DCP (10 ppm).

## 1. Introduction

Photocatalysis with semiconductor materials is a proven mechanism for the potential removal of environmental organic pollutants.<sup>1–5</sup> Compared with binary oxide photocatalysts, the more common ternary oxides often have multiple band energies and favorable stability in acidic and basic solutions, allowing them to be suitable for photocatalysis under various light sources and reaction conditions. A number of ternary oxides, such as  $\text{Bi}_2\text{WO}_6$ ,<sup>6,7</sup>  $\text{ZnFe}_2\text{O}_4$ ,<sup>8</sup> and  $\text{CdWO}_4$ ,<sup>9</sup> have been tested in photocatalytic applications under visible or ultraviolet (UV) light irradiation. Zinc stannate, an important ternary oxide, has been widely investigated as a candidate material for gas sensors,<sup>10,11</sup> electrical devices,<sup>12,13</sup> and Li-ion battery applications.<sup>14</sup> However, few efforts have been devoted to the evaluation of the photocatalytic applications of zinc stannate.<sup>15,16</sup>

Laser ablation in liquids (LAL) has proven to be a unique and efficient technique to generate and fragment metal, semiconductor, and ceramic nanoparticles.<sup>17</sup> Moreover, the highly reactive and metastable nanomaterials obtained by laser ablation in liquid can be further utilized for the extended assembly of advanced functional materials in aging, electrodeposition or hydrothermal treatment processes.<sup>18–21</sup>

In contrast with traditional techniques, such as the solid-state reaction, co-precipitation, and solvothermal methods, we report

here a new strategy for the synthesis of zinc stannate nanocubes and nanourchins by a combined strategy of LAL and hydrothermal treatment. Highly reactive  $\text{SnO}_x$  and  $\text{ZnO}_x(\text{OH})_y$  colloidal precursors were first generated by laser ablation of Sn and Zn targets in deionized water, the mixture of which was hydrothermally treated by the addition of ammonia. The final morphology and phase of the synthesized zinc stannate can be modulated by the addition of ammonia such that  $\text{Zn}_2\text{SnO}_4$  nanocubes were obtained without the use of ammonia, while Zn-deficient  $\text{ZnSnO}_3$  nanourchins were obtained at a high ammonia concentration of  $3.0 \text{ mol L}^{-1}$ . Methyl orange (MO) and 2,5-dichlorophenol (2,5-DCP) were used as model pollutants to evaluate the photocatalytic activity of nanourchin  $\text{ZnSnO}_3$  under UV light irradiation. Highly concentrated MO (25 ppm) and 2,5-DCP (10 ppm) aqueous solutions can be quickly decomposed by the addition of the nanourchins at a relatively low concentration of  $30 \text{ mg L}^{-1}$ .

## 2. Materials and methods

2.1 LAL-induced  $\text{ZnO}_x(\text{OH})_y$  and  $\text{SnO}_x$  colloidal precursors

The typical preparation procedures are as follows: a zinc plate with 99.99% purity was fixed onto a supporter in a vessel that was filled with 12 mL of deionized water. The vessel was then installed onto a controlled turntable, which was set to rotate continuously (10 rpm). The metal plate was ablated for 15 min by a fundamental Nd:YAG laser (1064 nm) with a 10 Hz pulse repetition rate, 6 ns pulse duration, and 100 mJ per pulse energy density. Generated colloidal solutions were collected and kept in a container for further hydrothermal treatment. The preparation of Sn colloids was also done in a

Key Laboratory of Materials Physics and Anhui Key Laboratory of Nanomaterials and Nanotechnology, Institute of Solid State Physics, Hefei Institutes of Physical Science, Chinese Academy of Sciences, Hefei, 230031, P. R. China. E-mail: chliang@issp.ac.cn; Fax: +86-551-5591434; Tel: +86-551-5591129

† Electronic supplementary information (ESI) available. See DOI: 10.1039/c2jm32406g

similar manner, but instead of a zinc plate, the ablation step was done with a tin plate (99.99% purity) in 12 mL of deionized water.

## 2.2 Assembly of $\text{ZnSnO}_3$ and $\text{Zn}_2\text{SnO}_4$ nanocubes and nanourchins

$\text{ZnO}_x(\text{OH})_y$  and  $\text{SnO}_x$  colloids were mixed at a volume ratio of 1 : 1 and then divided into equal volumes of 35 mL. A strong ammonia solution (28%) was added to the LAL-generated colloids with vigorous stirring. The final volume of the reaction mixture was adjusted to 45 mL with deionized water before it was transferred into a 60 mL autoclave with an inner Teflon lining and incubated at 180 °C for 15 h. After reaction, the products were collected by centrifugation, thoroughly washed with deionized water and absolute alcohol, and then dried in an oven at 40 °C for 12 h.

## 2.3 Structural and morphological characterization

The morphology of the as-synthesized products was investigated by field emission scanning electron microscopy (SEM, Sirion 200). Powder X-ray diffraction (XRD) patterns of the synthesized products were collected using a Philips X'Pert system with Cu-K $\alpha$  radiation ( $\lambda = 1.5419 \text{ \AA}$ ). The optical absorption of the colloidal products was monitored by using an ultraviolet-visible (UV-vis) spectrophotometer (Shimadzu UV-2550). Surface chemical constituents of the products were analyzed by X-ray photoelectron spectroscopy (XPS; Thermo ESCALB 250). A small amount of the powdered product was dispersed in ethanol to form a suspension, a drop of which was then dipped onto a carbon-coated Cu grid for specimen investigation by transmission electron microscopy (TEM, JEOL-2010) with an accelerating voltage of 200 kV.

## 2.4 Photocatalytic activity assessment

MO and 2,5-DCP aqueous solutions were used to evaluate the photocatalytic activity of  $\text{ZnSnO}_3$  nanourchins in response to UV light illumination at room temperature. The experiment of MO degradation was done as follows: two glass culture dishes, each of which was 6.5 cm inner diameter, containing 30 mL of MO aqueous solution (25 mg  $\text{L}^{-1}$ , pH = 3.0) were first prepared. Then, the dried  $\text{ZnSnO}_3$  powder was added to one culture dish at a final concentration of 30 mg  $\text{L}^{-1}$ ; the other dish was used as a control treatment for comparison. The culture dishes were placed in a dark chamber for 1 h before they were placed under UV illumination. Two UV lamps (15 W), with wavelengths centered at 254 nm and an energy intensity of 1100  $\mu\text{W cm}^{-2}$  (25 cm distance from lamps), were used as the light source to excite the photocatalytic reactions. A fixed volume of the MO solution was regularly collected by centrifugation, and the concentration of MO was monitored using a UV-vis spectrophotometer. The decomposition of MO (25 mg  $\text{L}^{-1}$ , pH = 6.4) and 2,5-DCP (10 mg  $\text{L}^{-1}$ , pH = 6.4) was analyzed by similar procedures.

## 3. Results and discussion

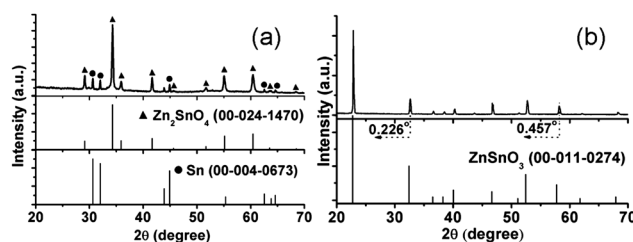
### 3.1 Zinc stannate phases by XRD analysis

XRD peaks of the mixture of LAL-generated  $\text{ZnO}_x(\text{OH})_y$  and  $\text{SnO}_x$  colloidal solutions could be well indexed to the  $\text{Zn}_2\text{SnO}_4$  (JCPDS no. 00-024-1470) phase even without the addition of ammonia, except for several weak peaks ascribed to the metal Sn phase (JCPDS no. 00-004-0673), as shown in Fig. 1a. As ammonia was added in gradually increasing amounts, the metal Sn phase disappeared, and zinc stannate in the  $\text{ZnSnO}_3$  phase became the main component, as depicted in Fig. S2†. When the molar volume of ammonia exceeded 0.3 mol  $\text{L}^{-1}$ , the  $\text{Zn}_2\text{SnO}_4$  phase also disappeared. Fig. 1b presents the XRD pattern of the final product obtained at an ammonia concentration of 3.0 mol  $\text{L}^{-1}$ . The peak positions and intensities observed were similar to those of the zinc stannate  $\text{ZnSnO}_3$  phase (JCPDS no. 00-011-0274), but the peak locations presented a slight shift to larger angles ( $2\theta$ ) with a noticeable difference in values. For example, the peaks located at 32.412° and 57.716° in  $2\theta$  of  $\text{ZnSnO}_3$  shifted to positions 32.638° and 58.173° in the present product. Increases of 0.226° and 0.457° indicate lattice distortions of 0.017 Å and 0.011 Å in the (220) and (422) crystalline planes, respectively. XRD analysis demonstrates that the phase structure of the synthesized product was remarkably affected by the amount of ammonia added.

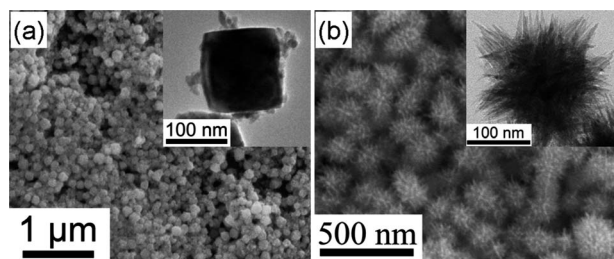
### 3.2 Morphologies of zinc stannate nanostructures

Fig. 2 presents typical SEM and homologous TEM images of the synthesized samples. Fig. 2a shows two typical morphologies of the products synthesized without the addition of ammonia: a cube-like structure with an average size of 150 nm and much smaller nanocrystals with sizes of around 10 nm. When ammonia was added to the reaction, especially at high concentrations, pure and uniform urchin-like  $\text{ZnSnO}_3$  with sizes of 200 nm could be generated, as shown in Fig. 2b. If the amount of ammonia was varied within the range of 0.30 mol  $\text{L}^{-1}$  to 3.0 mol  $\text{L}^{-1}$ , only the  $\text{ZnSnO}_3$  phase was produced; however, the morphologies of the products varied greatly (Fig. S3†). At low ammonia concentrations (0.15 mol  $\text{L}^{-1}$  or 0.30 mol  $\text{L}^{-1}$ ), the products presented irregular shapes. At 0.6 mol  $\text{L}^{-1}$  ammonia, nanoplate-like shapes with nanorods attached to the edges were observed. As the added amount of ammonia increased to 1.5 mol  $\text{L}^{-1}$ , the product morphology became similar to that synthesized with 3.0 mol  $\text{L}^{-1}$ , as shown in Fig. S2†.

Further structural investigation of the zinc stannate nanostructures was done by high-resolution TEM (HRTEM). For



**Fig. 1** XRD patterns of the tunable zinc stannate phases by changing the concentration of the added ammonia: (a) 0 mol  $\text{L}^{-1}$  and (b) 3.0 mol  $\text{L}^{-1}$ .



**Fig. 2** SEM and TEM images of as-synthesized zinc stannate nanostructures with different amounts of ammonia added: (a) 0 mol L<sup>-1</sup> and (b) 3.0 mol L<sup>-1</sup>.

the sample with no ammonia added, the product was mainly composed of cube-like nanoparticles. As shown in Fig. 3a, the interplanar distance (0.50 nm) agreed with the lattice spacing of the (111) plane of the Zn<sub>2</sub>SnO<sub>4</sub> phase. When ammonia was used as the reaction reagent, the ZnSnO<sub>3</sub> phase was obtained (Fig. 1b). However, the measured 0.354 nm interplanar distance of the single nanourchins (Fig. 3b) did not agree well with that of ZnSnO<sub>3</sub> (0.391 nm). Obvious lattice distortion was also found to occur with this technique of deriving ZnSnO<sub>3</sub> nanostructures.

### 3.3 Surface chemical states of ZnSnO<sub>3</sub> nanourchins

Fig. 4 shows the typical XPS valance band spectra of Zn and Sn in the ZnSnO<sub>3</sub> nanourchin sample. The Zn 2p scan (Fig. 4a) shows that the binding energy of Zn 2p<sub>3/2</sub> (1021.5 eV) deviates from the reported value of 1022.7 eV for the ZnSnO<sub>3</sub> phase.<sup>22</sup> This deviation occurs also for the Sn 3d scan (Fig. 4b). The binding energies of Sn 3d<sub>5/2</sub> and Sn 3d<sub>3/2</sub> decreased from 487.0 eV and 496.6 eV (reported phase) to 486.2 eV and 494.7 eV (nanourchin phase), respectively. The obvious decrease of the Zn 2p and Sn 3d binding energies has been often observed in Zn-doped SnO<sub>2</sub> structures.<sup>23–25</sup> These results can be attributed to the oxygen-deficient formation that decreases the binding energy of Sn. Moreover, in contrast to the reported 20 atom.% heavy doping of Zn in SnO<sub>2</sub> that does not give information on the secondary phase,<sup>26</sup> our calculations from the XPS spectra indicate that the ratio of the surface elements Sn : Zn : O is about 1 : 0.45 : 2.82, and the final product exists as the perovskite ZnSnO<sub>3</sub> phase.

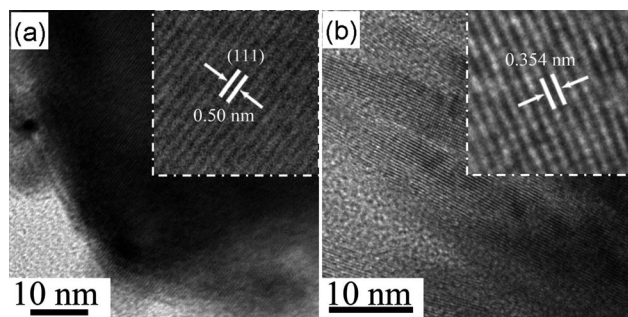


**Fig. 3** Typical HRTEM images of (a) ZnSnO<sub>4</sub> nanocube and (b) ZnSnO<sub>3</sub> nanourchin nanostructures.

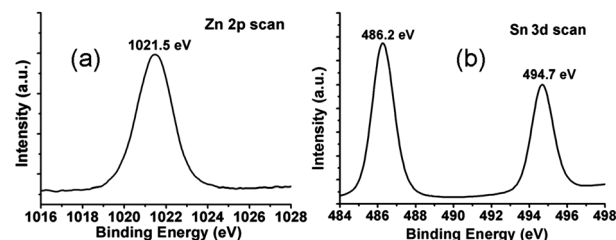
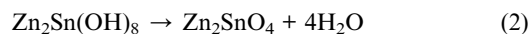
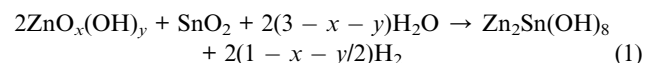


**Fig. 4** XPS valance band spectra of ZnSnO<sub>3</sub> nanourchins: (a) Zn 2p scan; and (b) Sn 3d scan.

### 3.4 Growth processes of zinc stannate nanostructures

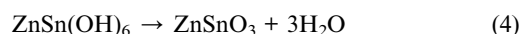
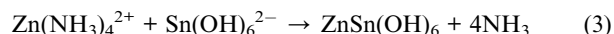
The freshly derived colloids produced by the LAL of Zn in pure water were mainly composed of ZnO, and Zn(OH)<sub>2</sub> with a small amount of Zn nanoparticles (described as ZnO<sub>x</sub>(OH)<sub>y</sub>). The properties of the Sn colloids have been systematically investigated in our earlier work.<sup>27</sup> A detailed characterization of the product morphologies and phases is given in Fig. S1†.

When the two colloids are mixed and heated in the absence of ammonia, the following reactions take place:



Under hydrothermal conditions (180 °C), metallic Zn ( $x, y = 0, 0$  for ZnO<sub>x</sub>(OH)<sub>y</sub>) can be involved in reaction (1). However, it is difficult for metallic Sn ( $x = 0$  for SnO<sub>x</sub>) to react in such conditions; thus, the Sn phase is still detected by XRD analysis, as shown in Fig. 1a.

Upon the addition of ammonia, the ZnO<sub>x</sub>(OH)<sub>y</sub> and SnO<sub>x</sub> nanomaterials in the colloid mixture react with NH<sub>4</sub><sup>+</sup> and OH<sup>-</sup>, thus generating the complex ions of Zn(NH<sub>3</sub>)<sub>4</sub><sup>2+</sup> and Sn(OH)<sub>6</sub><sup>2-</sup>:



In basic solutions, the etching actions of ZnSn(OH)<sub>6</sub> that accompany reaction (3) should be considered. Studies of Zn-doped SnO<sub>2</sub> or Zn-poor Zn<sub>2</sub>SnO<sub>4</sub> show that ZnSn(OH)<sub>6</sub> produced in the initial stages is etched by OH<sup>-</sup> to form the target product.<sup>23</sup> In this study, the tin oxide phase represented by Zn-doped SnO<sub>2</sub> (Sn<sub>1-x</sub>Zn<sub>x</sub>O<sub>2</sub>) was found with prolonged reaction times, as shown in Fig. 5b and c. The XRD pattern also shows sharp peaks belonging to the perovskite ZnSnO<sub>3</sub> phase. For Zn-deficient ZnSnO<sub>3</sub>, the interplanar spacing is still 0.354 nm, whereas for Zn-doped SnO<sub>2</sub>, the spacing decreases to 0.343 nm.

### 3.5 Optical and electrochemical properties of ZnSnO<sub>3</sub> nanourchins

An FTO glass substrate coated with the Zn-deficient ZnSnO<sub>3</sub> film was prepared (see ESI†) to test its electrochemical properties. Generally, the flat band potential can be determined by the capacitance measurement of the electrode–electrolyte interface with the help of a Mott–Schottky plot. Fig. 6a shows the



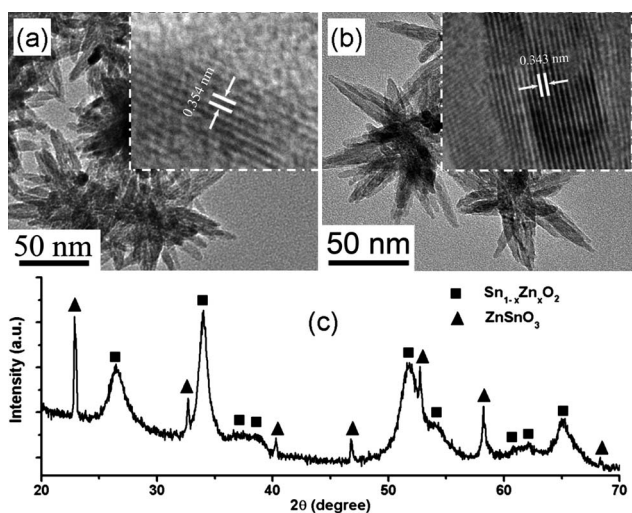


Fig. 5 Sample characterization by hydrothermal treatment for 20 h: (a), (b) TEM and HRTEM images; and (c) the XRD pattern.

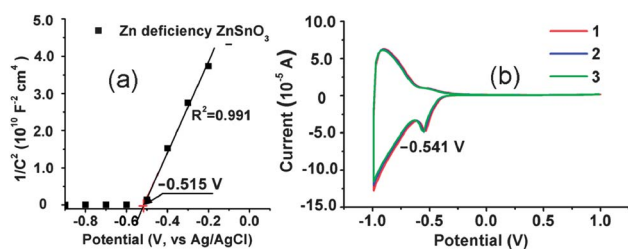


Fig. 6 Electrochemical characteristics of the ZnSnO<sub>3</sub> electrode measured at an AC frequency of 1000 Hz in 0.1 mol L<sup>-1</sup> Na<sub>2</sub>SO<sub>4</sub>: (a) Mott-Schottky plots; and (b) cyclic voltammograms.

Mott-Schottky plots of the ZnSnO<sub>3</sub> nanourchins measured at an AC frequency of 1000 Hz. The positive slope from the Mott-Schottky plots indicates that the sample is an n-type semiconductor. The flat band potential measured from the intercept of this plot was  $-0.515$  V (vs. Ag/AgCl), which is close to the cathodic peak value (bottom of the conduction band) located at  $-0.541$  V (vs. Ag/AgCl) in the cyclic voltammograms shown in Fig. 6b. After three cycles of measurement, the surface state of the film electrode was still stable.

A small amount of synthesized ZnSnO<sub>3</sub> was well dispersed in water to form a homogeneous suspension. The absorption

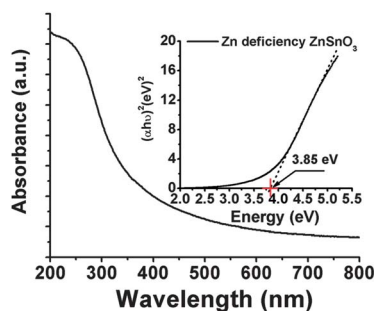


Fig. 7 Absorbance spectrum and band energy of the prepared urchin-like ZnSnO<sub>3</sub> samples.

spectrum and corresponding band gap calculations (inset) are shown in Fig. 7. An estimate of the optical band gap was obtained by using the following equation:<sup>28</sup>

$$A = \frac{K(h\nu - E_g)^{n/2}}{h\nu} \quad (5)$$

Where,  $A$  is the absorbance,  $K$  is a constant, and  $n$  equals 1 for direct transition or 2 for indirect transition. Here,  $n = 1$  and the band gap of the as-prepared Zn-deficient ZnSnO<sub>3</sub> was estimated to be 3.85 eV.

### 3.6 Photocatalysis decomposition of MO and 2,5-DCP

Fig. 8a intuitively displays MO degradation by ZnSnO<sub>3</sub> nanourchins. Curves a, b, c, and d in Fig. 8b present the time-dependent degradation of MO using ZnSnO<sub>3</sub> compared with a blank solution and P25. Without any catalyst (curve a), the degradation process under UV-light irradiation is negligible. Upon addition of the ZnSnO<sub>3</sub> nanourchins, MO was decomposed in both neutral and acidic conditions (curves b and d). More importantly, the ZnSnO<sub>3</sub> nanourchins rapidly decomposed MO in acidic conditions (pH = 3.0) at a rate that was faster than that of Degussa P25 TiO<sub>2</sub> (curve c). The degradation amount could exceed 98% after 90 min of reaction. Chlorophenols can spontaneously decompose under UV irradiation. In this study, about 34% of the 2,5-DCP remained under UV-light irradiation for 120 min without the use of the ZnSnO<sub>3</sub> catalyst, as shown in curve a (Fig. 8d). When ZnSnO<sub>3</sub> nanourchins were used, the degradation progress of 2,5-DCP was accelerated (Fig. 8d, curve b) and more than 95% of the 2,5-DCP was decomposed. Comparing the peaks in the local enlarged UV spectra shown in Fig. S4a and S4b†, the B-band derived from the benzene ring disappears with the addition of the ZnSnO<sub>3</sub> catalyst but remains if the catalyst is not used. The disappearance of the B-band indicates that the benzene ring is destroyed and that ZnSnO<sub>3</sub> can prompt the complete decomposition of 2,5-DCP.

The ZnSnO<sub>3</sub> nanourchins showed high activity for the decomposition of MO and 2,5-DCP. MO and 2,5-DCP degradation follows a first-order kinetic model in the presence

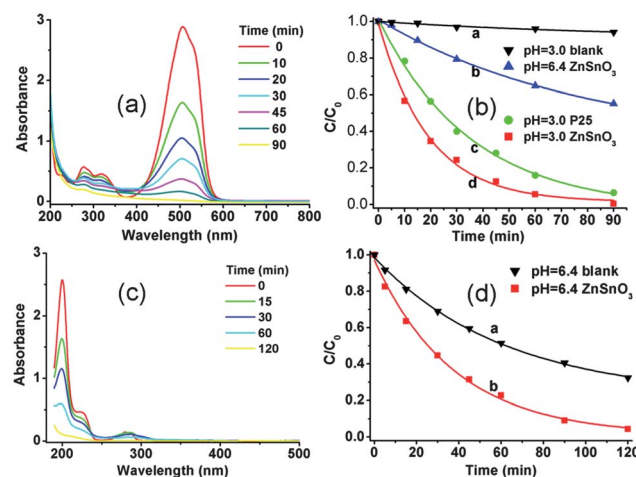


Fig. 8 UV spectra of (a) methyl orange and (c) 2,5-DCP degradation under UV-light irradiation, with the corresponding normalization concentration of (b) methyl orange and (d) 2,5-DCP.

of  $\text{ZnSnO}_3$ , the results of which are shown in Fig. 8b and d (solid lines).

#### 4. Conclusions

In summary, we developed a new synthesis route to obtain zinc stannate nanophotocatalysts. LAL-induced Zn and Sn colloids were used as chemical-friendly precursors to synthesize  $\text{Zn}_2\text{SnO}_4$  and  $\text{ZnSnO}_3$  in a hydrothermal treatment process. Cubic spinel-type  $\text{Zn}_2\text{SnO}_4$  was produced in neutral solution while Zn-deficient  $\text{ZnSnO}_3$  was synthesized in basic solution. The morphology of  $\text{ZnSnO}_3$  can be modulated by changing the ammonia concentration. Unavoidable etching in the basic solution results in the production of Zn-deficient  $\text{ZnSnO}_3$ . Zn-deficient  $\text{ZnSnO}_3$  is an n-type semiconductor with a large band gap of 3.85 eV that presents good dispersibility, high stability, and high photocatalytic effectiveness for MO and 2,5-DCP degradation.

#### Acknowledgements

This research was supported by the National Natural Science Foundation of China (NSFC, no.10974204, 50931002) and the Hundred Talent Program of the Chinese Academy of Sciences (CAS). The authors also thank: X. Zhu, L. Chen, M. Kong for their expertise with instrumentation.

#### References

- 1 M. R. Hoffmann, S. T. Martin, W. Y. Choi and D. W. Bahnemann, *Chem. Rev.*, 1995, **95**, 69–96.
- 2 S. S. Wu, H. Q. Cao, S. F. Yin, X. W. Liu and X. R. Zhang, *J. Phys. Chem. C*, 2009, **113**, 17893–17898.
- 3 S. P. Albu, A. Ghicov, J. M. Macak, R. Hahn and P. Schmuki, *Nano Lett.*, 2007, **7**, 1286–1289.
- 4 R. Asahi, T. Morikawa, T. Ohwaki, K. Aoki and Y. Taga, *Science*, 2001, **293**, 269–271.
- 5 K. Lee, D. Kim, P. Roy, I. Paramasivam, B. I. Birajdar, E. Spiecker and P. Schmuki, *J. Am. Chem. Soc.*, 2010, **132**, 1478–1479.
- 6 L. S. Zhang, W. Z. Wang, L. Zhou and H. L. Xu, *Small*, 2007, **3**, 1618–1625.
- 7 C. Zhang and Y. F. Zhu, *Chem. Mater.*, 2005, **17**, 3537–3545.
- 8 X. Y. Li, Y. Hou, Q. D. Zhao, W. Teng, X. J. Hu and G. H. Chen, *Chemosphere*, 2011, **82**, 581–586.
- 9 W. M. Tong, L. P. Li, W. B. Hu, T. J. Yan and G. S. Li, *J. Phys. Chem. C*, 2010, **114**, 1512–1519.
- 10 B. Y. Geng, C. H. Fang, F. M. Zhan and N. Yu, *Small*, 2008, **4**, 1337–1343.
- 11 Y. Zeng, T. Zhang, H. T. Fan, W. Y. Fu, G. Y. Lu, Y. M. Sui and H. B. Yang, *J. Phys. Chem. C*, 2009, **113**, 19000–19004.
- 12 M. Miyauchi, Z. F. Liu, Z. G. Zhao, S. Anandan and K. Hara, *Chem. Commun.*, 2010, **46**, 1529–1531.
- 13 T. Lana-Villarreal, G. Boschloo and A. Hagfeldt, *J. Phys. Chem. C*, 2007, **111**, 5549–5556.
- 14 A. Rong, X. P. Gao, G. R. Li, T. Y. Yan, H. Y. Zhu, J. Q. Qu and D. Y. Song, *J. Phys. Chem. B*, 2006, **110**, 14754–14760.
- 15 C. H. Fang, B. Y. Geng, J. Liu and F. M. Zhan, *Chem. Commun.*, 2009, 2350–2352.
- 16 X. L. Fu, X. X. Wang, J. L. Long, Z. X. Ding, T. J. Yan, G. Y. Zhang, Z. Z. Zhang, H. X. Lin and X. Z. Fu, *J. Solid State Chem.*, 2009, **182**, 517–524.
- 17 G. W. Yang, *Prog. Mater. Sci.*, 2007, **52**, 648–698.
- 18 J. Liu, C. H. Liang, H. M. Zhang, S. Y. Zhang and Z. F. Tian, *Chem. Commun.*, 2011, **47**, 8040–8042.
- 19 H. M. Zhang, C. H. Liang, Z. F. Tian, G. Z. Wang and W. P. Cai, *CrystEngComm*, 2011, **13**, 1063–1066.
- 20 H. He, W. P. Cai, Y. X. Lin and B. S. Chen, *Chem. Commun.*, 2010, **46**, 7223–7225.
- 21 C. He, T. Sasaki, Y. Shimizu and N. Koshizaki, *Appl. Surf. Sci.*, 2008, **254**, 2196–2202.
- 22 T. Pan, M. H. Ma, F. B. Xin and X. Q. Xin, *Appl. Surf. Sci.*, 2001, **181**, 191–195.
- 23 X. C. Dou, D. Sabba, N. Mathews, L. H. Wong, Y. M. Lam and S. Mhaisalkar, *Chem. Mater.*, 2011, **23**, 3938–3945.
- 24 E. Ramasamy and J. Lee, *Energy Environ. Sci.*, 2011, **4**, 2529–2536.
- 25 G. Cheng, K. Wu, P. T. Zhao, Y. Cheng, X. L. He and K. X. Huang, *J. Cryst. Growth*, 2007, **309**, 53–59.
- 26 X. F. Liu, J. Iqbal, Z. B. Wu, B. He and R. H. Yu, *J. Phys. Chem. C*, 2010, **114**, 4790–4796.
- 27 Z. F. Tian, C. H. Liang, J. Liu, H. M. Zhang and L. D. Zhang, *J. Mater. Chem.*, 2011, **21**, 18242–18247.
- 28 D. P. Singh, N. R. Neti, A. S. K. Sinha and O. N. Srivastava, *J. Phys. Chem. C*, 2007, **111**, 1638–1645.